Check for updates

Efficient deoxygenation of waste cooking oil over Co₃O₄–La₂O₃-doped activated carbon for the production of diesel-like fuel†

G. Abdulkareem-Alsultan, [ID] *[abe] N. Asikin-Mijan, [ID] *[a] G. Mustafa-Alsultan,[f] H. V. Lee, [ID] [d] Karen Wilson [ID] [e] and Y. H. Taufiq-Yap*[ac]

Untreated waste cooking oil (WCO) with significant levels of water and fatty acids (FFAs) was deoxygenated over Co_3O_4–La_2O_3/AC_{nano} catalysts under an inert flow of N_2 in a micro-batch closed system for the production of green diesel. The primary reaction mechanism was found to be the decarbonylation/decarboxylation (deCOx) pathway in the Co_3O_4–La_2O_3/AC_{nano}-catalyzed reaction. The effect of cobalt doping, catalyst loading, different deoxygenation (DO) systems, temperature and time were investigated. The results indicated that among the various cobalt doping levels (between 5 and 25 wt%), the maximum catalytic activity was exhibited with the Co : La ratio of 20 : 20 wt/wt% DO under N_2 flow, which yielded 58% hydrocarbons with majority diesel-range (n-(C_{15} + C_{17})) selectivity (∼63%), using 3 wt% catalyst loading at a temperature of 350 °C within 180 min. Interestingly, 1 wt% of catalyst in the micro-batch closed system yielded 96% hydrocarbons with 93% n-(C_{15} + C_{17}) selectivity within 60 min at 330 °C, 38.4 wt% FFA and 5% water content. An examination of the WCO under a series of FFA (0–20%) and water contents (0.5–20 wt%) indicated an enhanced yield of green diesel, and increased involvement of the deCOx mechanism. A high water content was found to increase the decomposition of triglycerides into FFAs and promote the DO reaction. The present work demonstrates that WCO with significant levels of water and FFAs generated by the food industry can provide an economical and naturally replenished raw material for the production of diesel.

1. Introduction

A range of geopolitical, economic and environmental issues (*e.g.* global warming, diminishing petroleum deposits, increasing crude oil prices and demand for energy independence) have promoted recent interest in biofuels. Accordingly, fuels obtained from biomass (biofuels) are considered as a carbon-neutral and renewable substitute for fossil fuels. In particular, much attention has been paid to bio-oils, which can readily be obtained *via* the pyrolysis (thermal and catalytic cracking) of biomass. Nevertheless, the considerably low selectivity of this approach, which generates a range of unwanted products (primarily oxygenates), requires additional development. On the other hand, the well-established biofuel, which is known as biodiesel or fatty acid methyl esters (FAMEs), is composed of highly oxygenated compounds and suffer from several inevitable drawbacks such as poor storage stability and poor cold-flow behaviour.[1,2] Consequently, elimination of oxygen-bonded compounds is necessary to achieve desirable diesel properties. Significantly, the high oxygen content of biodiesel and bio-oils gives rise to most of their disadvantages, including a lower heat content than that of conventional fossil fuels. Thus, the production of (oxygen-free) hydrocarbons from the catalytic deoxygenation (DO) of fatty acids and their derivatives has attracted interest. In principle, DO involves oxygen extraction from fatty acids and their derivatives *via* decarboxylation ($-CO_2$) and decarbonylation ($-CO$, H_2O) (deCOx) reactions under an H_2-free atmosphere.

There are several solid acid catalysts containing metal sulfides, noble metals, metal phosphides, metal carbides, metals, and transition metal oxides with supporting materials reported for the DO reaction. Sulfonated acidic catalysts show high affinity toward the production of hydrocarbon fractions, but suffer from sulphur leaching and affect the quality of oil.[3,4]

[a]*Catalysis Science and Technology Research Centre (PutraCat), Faculty of Science, Universiti Putra Malaysia, 43400 UPM Serdang, Selangor, Malaysia. E-mail: taufiq@upm.edu.my; Fax: +603-89466758; Tel: +603-89466809*

[b]*Chemical and Environmental Engineering Department, Faculty of Engineering, Universiti Putra Malaysia, 43400 UPM Serdang, Selangor, Malaysia. E-mail: kreem. alsultan@yahoo.com; Tel: +601-82534058*

[c]*Chancellery Office, Universiti Malaysia Sabah, 88400, Kota Kinabalu, Sabah, Malaysia*

[d]*Nanotechnology & Catalysis Research Centre (NanoCat), Institute of Postgraduate Studies, University Malaya, 50603 Kuala Lumpur, Malaysia*

[e]*School of Science, RMIT University, Melbourne, VIC 3001, Australia*

[f]*Maintenance of Rotary Machine Equipment, South Refineries Company, Basra, Iraq*

† Electronic supplementary information (ESI) available. See DOI: 10.1039/c9ra09516k

Meanwhile, high acidity noble metal catalysts are costly,[5] which make them unattractive. Medium acidic catalysts, such as metal phosphates and carbides, and mesoporous catalysts, such as SBA-15, MCM-41, and HMS catalysts, are generally selected for biofuel production since they exhibit low affinity toward the deactivation of the catalyst together with high DO activity.[6] However, the complexity of their synthesis makes them unappealing.[7] Thus, the drawbacks of the above mentioned catalysts encourage the exploration of non-sulphated, low-cost, and facile catalysts for the production of high-quality renewable fuel.

The use of metal oxides in the DO reaction has been continuously reported and proven to be selective towards the formation of hydrocarbon fractions.[8] Common transition metal oxides (TMO) that are used in the DO process include Mn, Ni, Co, W, Mo, Cu, Fe and Zn. Among them, Co exhibits the highest rate of decarboxylation[9,10] and formation of rich-paraffin species. The enhancement of decarboxylation by Co is realized through its excellent acidic–basic properties.[11] Furthermore, Co also facilitates the formation of olefins (alkenes) *via* decarbonylation pathways, producing water as a by-product. However, water has a negative effect on Co, which is easily oxidized and deactivated. Recently, the incorporation of a Ca promoter in Co-supported SiO_2–Al_2O_3 led to substantial catalyst stability and suggested the stability of Co relies on the incorporation of a basic metal, where the basic metal promoter leads to the inhibition of water production by lowering the affinity for the decarbonylation reaction.[12] For instance, a report on the DO of waste cooking oil (WCO) *via* $deCO_x$ over acid-base catalysts (CaO–La_2O_3/AC_{nano} and Ag_2O_3–La_2O_3/AC_{nano}) recently disclosed that the basic sites in La_2O_3 play key role in the removal of C–O-bonded species *via* decarboxylation, and thereby lead to greater enhancement of the DO activity and product selectively toward n-(C_{15} + C_{17}) fractions.[3,12] Furthermore, the basic sites of La_2O_3 suppress coke colonization. Recently, Benito and co-workers examined the effect of the addition of La_2O_3 to Ni/Al_2O_3, and observed that La_2O_3 promotion led to increased catalyst longevity, probably due to the oxygen donation from $La_2O_2CO_3$ species to produce CO from carbon deposits.[13] Even though a series of binary oxide CaO–La_2O_3 and Ag_2O_3–La_2O_3-supported AC_{nano} have been studied in details,[3,12] their DO performance was unsatisfactory and rapidly deactivated by coke deposition. Based on previous findings, the incorporation of Co in La_2O_3/AC may be promising for the improvement in DO performance and the enhancement of anti-coking character. Furthermore, the use of Co_2O_3–La_3O_4 as a metal promoter on AC support has not been reported to date in the literature.

As is known, DO under an inert atmosphere is not beneficial for the formation of desired paraffins products. Green diesel consists of low mixtures of paraffin compounds, which are typically not beneficial for reducing NOx emission and possess a low cetane number. Furthermore, DO under an inert atmosphere prevents the production of a high mass of green diesel since the volatile liquids with non-condensable gases easily escape during the reaction. Thus, since the DO reaction atmosphere plays an important role in enhancing the formation of paraffins, in the present work, WCO was deoxygenized in a semi-batch inert flow reactor and micro-batch reactor over the binary oxide of Co_3O_4–La_2O_3 on AC_{nano} catalyst. The micro-batch reactor is a one-dimensional reactor (10 cm length × 0.8 cm diameter), providing rapid heat and high mass transfer rates.[14] Although the micro-batch reactor has been successfully utilized for the continuous operation of fast and highly exothermic reactions and transformations involving toxic and explosive chemicals such as hydrogenation, alkylation, oxidation, and polymerization,[15–17] this reactor system is rarely adopted in the DO reaction for the production of green diesel. Instead of varying the DO reactor set-up, the stoichiometric study of Co content (5–25 wt%), reaction time, catalyst loading, water and FFA content were explored. This study provides new insight into the interaction of Co_3O_4–La_2O_3 on AC_{nano} support and offer an alternative approach to curb coke deposition and improve the longevity of the catalyst during the DO reaction together with the formation of saturated hydrocarbon. The present work also provides new in-depth insight on the DO of WCO in inert and closed reaction systems.

2. Materials and methods

2.1 Materials

For the present study, the feedstock (palm oil-based WCO supplied by a restaurant at Serdang, Selangor, Malaysia) was used without purification. Table 1 summarises the characteristics of the crude WCO, including free fatty acid content and water content. The level of free fatty acids (18.4% by weight) is reflected by the total acid number (TAN) of 36.8 mg KOH g^{-1}. The fatty acid content of the WCO included the saturated palmitic (45.68%), stearic (4.25%) and myristic acid (1.3%), together with the unsaturated oleic (40.19%) and linoleic acid (7.90%). Anhydrous silver nitrate ($CoNO_3$, 99.99% pure) was supplied by Sigma Aldrich (UK), lanthanum nitrate hexahydrate (La (NO_3)$_3$·6H$_2$O, 99.0% pure) was supplied Merck (Germany), phosphoric acid (H_3PO_4, 85.0–87.0% pure) was supplied by J. T. Baker (USA), and Walnut shells (*Juglans* sp.) were obtained from a market in Basra (Iraq). Liquid alkane and alkene standards (n = C_8–C_{20}) for gas chromatographic analysis were supplied by Sigma Aldrich and used without additional purification. The

Table 1 Properties of the waste cooking oil (WCO) used as the reaction feedstock

Properties	Value
Density (g cm^{-3})	0.87
Viscosity (mm^2 s^{-1})	4.85
Moisture content (% wt)	1–5
Acid value (mg KOH g^{-1})	36.81
FFA content (%)	18.40
Fatty acid composition	
Myristic acid, C_{14}:0	1.93
Palmitic acid, C_{16}:0	45.68
Stearic acid, C_{18}:0	4.25
Oleic acid, C_{18}:1	40.19
Linoleic acid, C_{18}:2	7.95

internal standard was 1-bromohexane. GC-grade *n*-hexane, purity >98%, supplied by Merck (Germany), was used for dilution. N_2 gas with 99% purity was supplied by Linde Malaysia Sdn Bhd.

2.2 Catalyst preparation

A two-step process and additional treatment with H_3PO_4 were chosen for the preparation of activated carbons with a prolate shape, surface functionality and high purity. Initially, 50 g of dried walnut shell powder with a particle size in the range of 1–200 mesh was subjected to pyrolysis in an N_2 atmosphere at a heating rate of 5 °C min^{-1} up to 700 °C for 5 h. The sample was heated in a tube furnace using a ceramic vertical reactor. The carbonaceous product was activated by concentrated phosphoric acid at 158 °C for 12 h, then washed with hot water to pH = 7 and further dried in an oven overnight to form activated carbon (AC). The AC was then infused with 20 wt% La(NO$_3$)· 6H$_2$O and 5–30 wt% Co(NO$_3$) under continuous stirring for 6 h. The impregnation of the metal on the support was optimized *via* the vacuum impregnating procedure, and this was facilitated with a vacuum machine (Edwards RV12) at 6.3×10^{-6} mbar. Subsequently, a Stuart RE300DB rotary evaporator was employed for drying, under heating and reduced pressure for 3 h at 55 °C and −60 kPa, respectively. Subsequently, the AC-doped metals underwent calcination at 700 °C, which lasted for a 4 h period under an N_2 flow. The metal-doped AC was denoted as $Co_2O_{3(x)}$–$La_2O_{3(y)}/AC_{nano}$, where x = 5, 10, 15, 20, 25, and 30 wt%.

2.3 Material characterization

For the purpose of identifying the chemical composition and the state of dispersion of the metal-doped AC catalysts before and after the chemical reaction, X-ray diffraction (XRD) analysis was applied (Shimadzu, model XRD-6000). The Brunauer–Emmett–Teller (BET) technique was employed using an N_2 adsorption/desorption analyser (Thermo-Finnigan Sorpmatic 1990 series) to obtain information on the surface area, and pore size and volume distribution of the catalysts. Typically, the catalyst sample was degassed at a temperature of 150 °C overnight to eliminate foreign gases and moisture from the surface of the catalysts. The analysis was performed at −196 °C, and the desorption and adsorption of nitrogen (N_2) on the surface of the catalyst was performed in a vacuum chamber. Temperature-programmed desorption (TPD) was employed to examine the acidity and basicity of the catalysts. Here, two probe molecules, NH_3 and CO_2, were employed (TPD–CO_2 and TPD–NH_3, respectively). A Thermo Finnigan TPD/R/O 1100 instrument equipped with a thermal conductivity detector (TCD) was employed to conduct the examination. Typically, about 0.05 g of catalyst was pre-treated with an N_2 gas flow, which lasted for 30 min at a temperature of 250 °C. This process was followed by exposing the catalyst to CO_2 gas for adsorption within 1 h and flushing with N_2 gas to remove excess CO_2. Subsequently, CO_2 desorption from the basic sites of the catalyst was identified by using the TCD under a flow of helium gas (30 mL min^{-1}) in the temperature range of 50–900 °C. The temperature was kept

constant for 30 min. NH_3 adsorption/desorption was performed using similar steps as the TDP-CO_2 method. An electron microscope (LEO 1455 VP) was employed to record field-emission scanning electron microscopy (FESEM) images, which was equipped with energy dispersive X-ray (EDX) (facilitated by a Rayny EDX-720 spectrometer) to determine the elemental composition of the catalyst samples (P, Co, La, O and C). X-ray photoelectron spectroscopy (XPS) was used to study the chemical states on the surface of the Co_2O_3–La_2O_3/AC_{nano} sample, and measurements were performed with a Microprobe PHI Quantera II under ultrahigh vacuum (UHV) conditions (base vacuum of $\sim 10^{-8}$ Pa) at room temperature. For the X-ray source, radiation of Mg Kα ($h\nu$ = 1253.6 eV) was employed. Furthermore, thermal analysis using a thermogravimetry analyzer (TGA) (TGA 1000i, Instrument Specialists Inc, United States) was applied to identify the level of deposition of coke and carbon on the spent catalyst. Both the catalyst and spent catalyst were heated in the temperature range of 25–900 °C range (30 °C min^{-1}) with an airflow of 40 mL min^{-1}.

2.4 Catalytic deoxygenation of WCO

The DO of WCO was carried out in a 250 mL mechanically stirred semi-batch reactor. WCO ($\sim$10 g) was placed in the reactor together with 0.5 wt% of catalyst, and prior to the initiation of the experiment, inert N_2 gas was flushed into the reactor accompanied by continuous stirring of the mixture. The purpose of this process was to ensure that the O_2 and moisture from the air was eliminated before heat was applied. Afterwards, the mixture was continuously treated with a constant flow of N_2 (flow rate of 20 mL min^{-1}) at atmospheric pressure to maintain the inert conditions for the DO reaction. The DO reaction was performed at 300 °C for 1 h. A cooler was used to facilitate the condensation of the deoxygenated products, where the condensates were collected in a vessel of the batch reactor. After completing each experiment, the mixture was cooled to room temperature. For comparison, a 10 cm length and 0.8 cm diameter stainless steel tube was used as a micro batch reactor closed system, where initially, the catalyst and WCO were mixed and placed in the micro-reactor and then the system was flushed using nitrogen gas for 10 min with a flow of 3 mL min^{-1} and then the valve was closed and the reactor heated at a heating rate of 50 °C min^{-1} to the desired temperature, and after the reaction was finished, the system was cooled using ice-cold water. The mixture of catalyst, char and product were separated using a centrifuge (3500 rpm for 10 min). The final deoxygenated liquid products were further analysed by using gas chromatography with a flame ionization detector (GC-FID), gas chromatography-mass spectrometry (GC-MS) and Fourier-transform infrared spectroscopy.

2.5 Water and FFA content effect

The water and FFA contents have a direct effect on the DO reaction. Fatty acids are known to be the primary composition during the DO reaction of triglycerides. Therefore, oleic acid was chosen as a model reactant. The water content in WCO will affect hydrolysis process of TG, where the TG molecules split

into free fatty acids and propane. To vary the FFA content, the WCO used in this study consisted of average triglycerides of 92 wt%, free fatty acids of 6.6 wt%, and unknown impurities of 1.4 wt%. The feedstock was free of water. Additional water or free fatty acid (oleic acid) was mixed with the WCO to adjust the initial parameters for the reaction tests. The fatty acid composition of the WCO was evaluated according to the standard AOCS method (1997), F9a-44 (Table 1). The WCO consisted of C_{14}–C_{20} fatty acids with the majority being unsaturated C_{18}:1 (oleic acid) and saturated C_{16}:0 (palmitic acid).

2.6 Product analysis

The reaction was analysed using an Agilent 7890A gas chromatograph (GC) fitted with a flame-ionization detector and an HP-5 capillary column (30 m × 0.25 mm × 0.33 mm). The sample (1 mL) was injected with a split ratio of 10 : 1. The carrier gas was nitrogen with a flow rate of 11 mL min^{-1}. The injector temperature was 280 °C and the detector temperature was 300 °C. The oven was programmed to maintain a temperature of 40 °C for 4 min before ramping up to 280 °C at a rate of 10 °C min^{-1}, maintaining this final temperature for 5 min. The products of the reaction were identified by comparing the retention times on the gas chromatograph with known standards and by examining the fragmentation patterns on an Agilent 5970 mass spectrometric (MS) detector. Calibration curves were used to provide quantitative analysis for each compound of interest. The determination of hydrocarbon yield (X) on the catalyst performance was evaluated by GC-FID using eqn (1) as follows:[18]

$$\text{Hydrocarbon yield } (\%) = \frac{\sum n_o + \sum n_i}{\sum n_z} \times 100 \qquad (1)$$

where n_o = peak area of alkenes (C_8–C_{20}), n_i = area of alkanes, and n_z = area of the product. The hydrocarbon selectivity (S) of the deoxygenated products was determined using eqn (2).

$$\text{Hydrocarbon selectivity } (\%) = \frac{C_x}{\sum n_x} \times 100 \qquad (2)$$

where C_x = peak area of the desired hydrocarbon fraction and n_x = area of hydrocarbons. The uncertainties were determined by repeated experiments and were reported as standard deviations, with each data point representing the mean average result obtained from a minimum of three separate experiments.

3. Results and discussion

3.1 Characterization of $Co_3O_{4(x)}$–$La_2O_{3(y)}$/AC_{nano} catalysts

The FESEM images of the nanosized walnut shell-derived AC catalyst were presented in our recent report.[3] The result indicated the presence of nanocrystalline fibrous particles with a thickness in the range of 15–20 nm on the AC catalyst support. Interestingly, the FESEM images of the $Co_3O_{4(x)}$–$La_2O_{3(y)}$/AC_{nano} catalysts, where x = 5, 10, 15, 20, 25 wt% and y = 20 wt%, showed well-dispersed, needle-like particles with a long and thin slab of nano-structures (Fig. 1A–E). The particle length and diameter were within the range of 190–290 nm and 11–23 nm, respectively. A further increment in Co species led to the

formation of compact micro-sized agglomerates. Based on the EDX analysis, the white spherical particles are attributed to Co species (identified by EDX analysis), which decreased in size and disappeared with an increase in the content of Co species contents. The change in morphology at different Co loading was due to the dopant effect, and thus resulted in aggregation.[19] The needle-like structures were deformed as the Co aggregates grew excessively on the catalyst surface. Fig. 1F and Table 2 show the EDX analysis of the $Co_3O_{4(x)}$–$La_2O_{3(y)}$/AC_{nano} catalysts, which indicate the presence of C, O, P, La, and Co elements. Thus, the treatment of AC with H_3PO_4 resulted the presence of P,[20,21] while the successful surface impregnation of La and Co was reflected by the presence of the corresponding elements in the EDX analysis. According to Table 2, the atomic ratio of Co : La in the catalysts was consistent with the expected (x : y) values of 5 : 20, 10 : 20, 15 : 20, 20 : 20 and 25 : 20. Overall, each of the $Co_3O_{4(x)}$–$La_2O_{3(y)}$/AC_{nano} catalysts had a maximum carbon content of >39%, which is expected to provide outstanding mechanical properties for both stability and thermal catalytic activity during DO reactions.

Fig. 2A presents the XRD analysis of AC and $Co_3O_{4(x)}$–$La_2O_{3(y)}$/AC_{nano} catalysts. AC displayed a peak centred at 2θ = 25.0°, which indicates the presence of amorphous carbonaceous materials.[22] In the case of the $Co_3O_{4(x)}$–$La_2O_{3(y)}$/AC_{nano} catalysts, the amorphous AC was altered to a highly crystalline state after the incorporation of the Co–La metals. Here, the XRD analysis revealed peaks at 2θ = 9.1°, 17.1°, 31.5°, 36.7°, 43.1°, 54.5°, 59.3° and 62.7°, which correspond to the Co_3O_4 phase (JCPDS File no. 00-001-1152).[23] The XRD peaks at 2θ = 14.1°, 18.1°, 25.3°, 26.6°, 29.6°, 39.2°, 46.6°, 54.6°, and 77.6° are attributed to the La_2O_3 phase (JCPDS File no. 00-037-1497).[24,25] The highly crystalline nature of the $Co_3O_{4(x)}$–$La_2O_{3(y)}$/AC_{nano} catalyst is due to the intercalation of La and Co ions in the AC matrix.[26,27] Upon increasing the Co dosage (from 5 to 25 wt%), the occurrence of bimetallic lanthanum cobalt oxide phases ($CoLaO_3$) at 2θ = 23.3°, 40.2° and 69.9° (JCPDS File no. 00-006-0491)[28,29] (Fig. 2B and C) evidenced the effective integration of the bimetallic (Co–La) structure into the AC_{nano} catalyst. Moreover, the bimetallic $CoLaO_3$ peaks corresponding to the (110)^1 plane gradually shifted to a lower angle with an increase in the Co content. This phenomenon indicates that more Co atoms were located deep in the La_2O_3 lattice with an increase in the Co content, indicating that the higher the Co content, the higher the amount of Co–LaO_3 solid solution is formed.[2] The homogeneous substitution of Co with La easily occurred because the radius of La^{3+} (1.16 Å) is larger than that of Co^{2+} (0.65 Å). Also the incorporation of Co-rich species in the $Co_3O_{4(x)}$–$La_2O_{3(y)}$/AC_{nano} catalyst promoted the dispersion of $CoLaO_3$ and reduced the crystallinity of $CoLaO_3$.[3,4] The present finding is consistent with the EDX results, where the oxygen content was reduced by 54% after the incorporation of 25 wt% of Co species (Table 2). Although the atomic radius of oxygen (1.67 Å) is larger than that of Co (0.65 Å), excess replacement by Co increased the size of the unit cell for $CoLaO_3$.[11] The increment in the average crystallite size for the $Co_3O_{4(x)}$–$La_2O_{3(y)}$/AC_{nano} catalyst with an increase in Co dosage is depicted in Table 3.
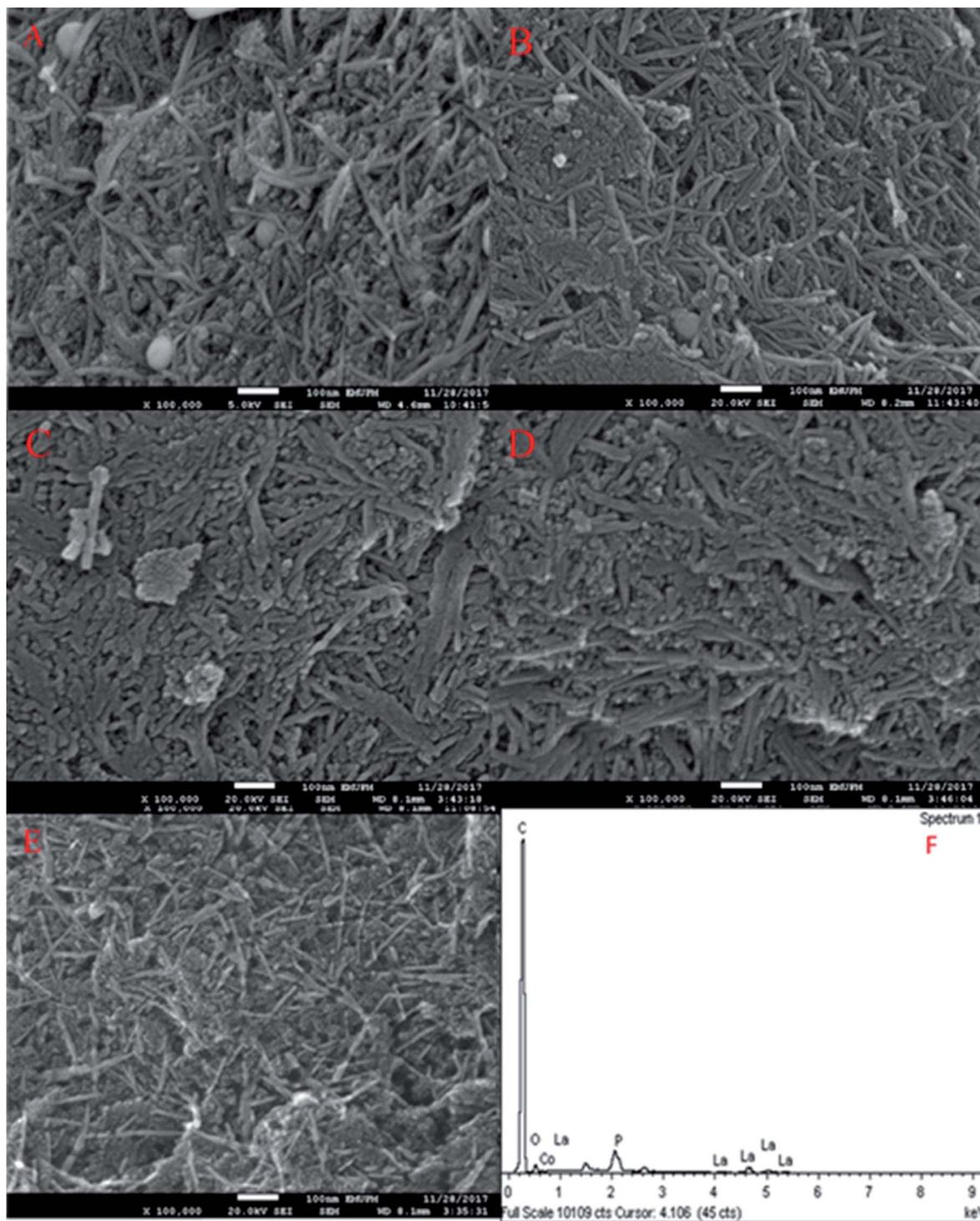
Fig. 1 FESEM images of (A) $Co_3O_{4(5\%)}$–$La_2O_{3(20\%)}$/AC_{nano}, (B) $Co_3O_{4(10\%)}$–$La_2O_{3(20\%)}$/AC_{nano}, (C) $Co_3O_{4(15\%)}$–$La_2O_{3(20\%)}$/AC_{nano}, (D) $Co_3O_{4(20\%)}$–$La_2O_{3(20\%)}$/AC_{nano}, and (E) $Co_3O_{4(25\%)}$–$La_2O_{3(20\%)}$/AC_{nano} catalysts and (F) EDX spectra for $Co_3O_{4(20\%)}$–$La_2O_{3(20\%)}$/AC_{nano} catalyst.

Table 3 lists the BET surface area for the $Co_3O_{4(x)}$–$La_2O_{3(20)}$/AC_{nano} catalysts with different Co : La ratios. The results indicate a decrease in the BET surface area from 668 to 486 $m^2\ g^{-1}$ with an increase in Co dosage from 5 to 25 wt%. The reduction in surface area with an increment in the Co content is due to the destruction of the needle-like structure together with the

formation of excessive small aggregates (see FESEM image), which covered the active sites of the catalyst surface.[30–32] Moreover, the pore volume of the $Co_3O_{4(x)}$–$La_2O_{3(20)}$/AC_{nano} catalyst decreased from 0.64 to 0.41 nm with an increase in Co content. These observations are attributed to the incorporation

Table 2 Catalyst element composition determined by energy-dispersive X-ray spectroscopy (EDS)

Catalyst[a]	Element composition[b] (%)				
	C	O	P	La	Co
$Co_3O_{4(5)}$–$La_2O_{3(20\%)}$/AC_{nano}	52.44	11.74	12.71	18.73	4.38
$Co_3O_{4(10)}$–$La_2O_{3(20\%)}$/AC_{nano}	49.37	10.46	9.27	19.60	11.30
$Co_3O_{4(15)}$–$La_2O_{3(20\%)}$/AC_{nano}	47.63	9.40	9.24	18.39	15.34
$Co_3O_{4(20)}$–$La_2O_{3(20\%)}$/AC_{nano}	43.16	8.43	10.21	19.23	18.97
$Co_3O_{4(25)}$–$La_2O_{3(20\%)}$/AC_{nano}	38.98	5.31	9.47	19.50	26.74

[a] Theoretical Co/La atomic ratio of catalyst. [b] Experimental Co/La atomic ratio in the synthesized catalyst determined by EDX.

of excess active metals (Co and La) in the pores of the AC support, which slightly blocked the porous structure.[24]

Previous work reported that acidic sites are necessary for enhancing the C–O and C–C bond cleavage *via* decarboxylation/decarbonylation and cracking pathways.[33] Besides acidic sites, basic sites play an important role in promoting decarboxylation and suppressing the formation of coke by reducing the deactivation rate of acidic catalysts.[34,35] Hence, the perfect and ideal DO catalyst can be achieved *via* the co-existence of basic and acidic sites. Thus, the acidity and basicity profiles for the $Co_3O_{4(x)}$–$La_2O_{3(y)}$/AC_{nano} catalyst were quantified by temperature-programmed desorption NH_3 (TPD-NH_3) and CO_2 desorption (TPD-CO_2) analyses, and the results are displayed in Fig. 3A and B and Table 3. The TPD–NH_3 profiles in Fig. 3A display two distinct NH_3 desorption peaks at temperatures of <150 °C and >500 °C, which are associated with the weak and strong acidic sites, respectively.[36] An examination of Table 3 reveals that the increment of Co doping from 5 to 20 wt%

induced the generation of strong acidic sites, which suggests that the presence of Co-rich species enhances the strength of the acidic sites. However, a dramatic decrease in the concentration of strong acid sites was observed with a further increment in Co content to 25 wt%. This can be attributed to the structural changes caused by the high Co content, which led to damage of the mixed oxide structure (Fig. 1E). The highest acidity distribution (30 208.66 μmol g^{-1}) was observed at a Co content of 20 wt% with the maximum increase of approximately 28% over the $Co_3O_{4(5\%)}$–$La_2O_{3(20\%)}$/AC_{nano} catalyst. The weak acidity indeed showed negligible changes (148.74–254.21 μmol g^{-1}) for all the $Co_3O_{4(x)}$–$La_2O_{3(y)}$/AC_{nano} catalysts. The basicity (TPD–CO_2) profiles of the various $Co_3O_{4(x)}$–$La_2O_{3(y)}$/AC_{nano} catalysts are presented in Fig. 3B and Table 3. Each catalyst displayed the main desorption peak at a temperature of >500 °C, which is attributed to the interaction of CO_2 with the strong basic sites of the catalyst. Similar to the trend on the acidity profile, the strong basic site distribution was found to increase with an increase in Co dopant up to 20 wt%. It is generally acknowledged that the basicity content will improve with an increase in Co loading.[37–39] This is due to the synergistic effect between Co and La on the activated carbon surface.[40–43] However, excess Co dopant covers the active sites of La, and thus provides lower basicity. Consistent with this, a reduction in the distribution of basic sites (5292.06 μmol g^{-1}) was found on the $Co_3O_{4(25)}$–$La_2O_{3(20)}$/AC_{nano} catalyst. In summary, the $Co_3O_{4(20\%)}$–$La_2O_{3(20\%)}$/AC_{nano} catalyst exhibited the highest CO_2 desorption peaks at T_{max} = 939 °C with the maximum basic site distribution (5292.06 μmol g^{-1}). Considering the acidity and basicity, an excess of Co dopant (25 wt%) results in high saturation of the Co-active sites, consequently hindering the active sites of La. Since, the capacity to instigate C–O cleavage is directly related to a high distribution of acid and basic active
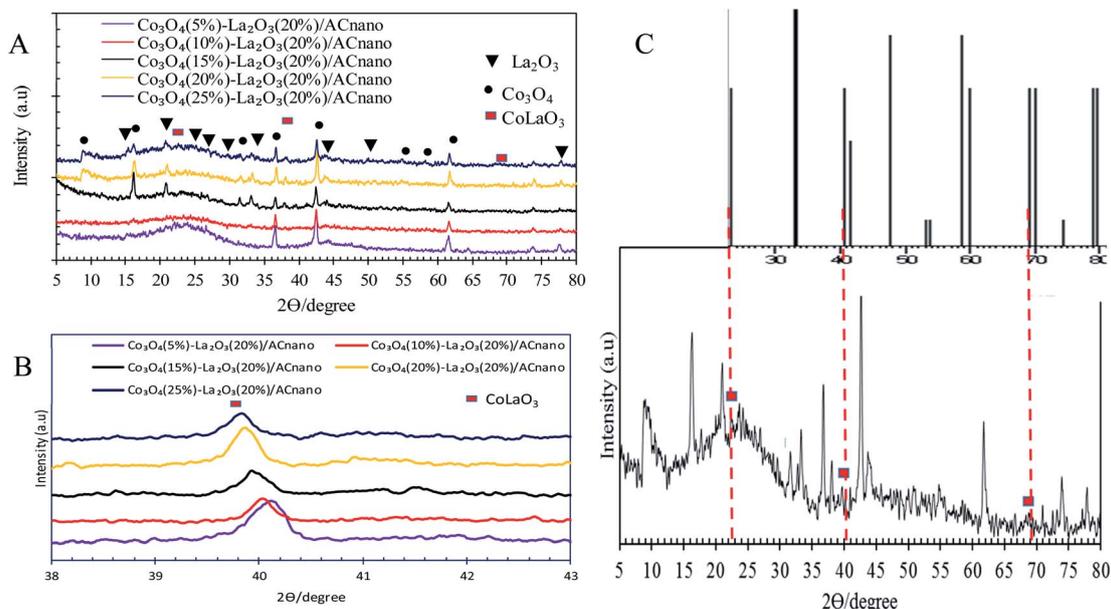

Fig. 2 (A) XRD patterns of $Co_3O_{4(x)}$–$La_2O_{3(20\%)}$/AC_{nano} catalysts, (B) bimetallic phase shifting and (C) bimetallic phase of $CoLa_2O_3$ of $Co_3O_{4(25)}$–$La_2O_{3(20\%)}$/AC_{nano} catalyst.

Table 3   Physicochemical properties of the $Co_3O_{4(x)}$-$La_2O_{3(y)}$/AC_{nano} catalysts

Catalyst	XRD[a] Crystallite size[a] (nm)	BET[b] Surface area[b] ($m^2\ g^{-1}$)	Pore volume[b] ($cm^3\ g^{-1}$)	TPD-NH$_3$[c] NH$_3$ desorption temperature[c] (°C)	Amount of NH$_3$ adsorbed[c] ($\mu mol\ g^{-1}$)	TPD-CO$_2$[c] CO$_2$ desorption temperature[c] (°C)	Amount of CO$_2$ adsorbed[c] ($\mu mol\ g^{-1}$)
$Co_3O_{4(5\%)}$–$La_2O_{3(20\%)}$/AC_{nano}	38.40	668.53	0.64	127/730/806	148.74/2584.76/19 266.00	635	3289.72
$Co_3O_{4(10\%)}$–$La_2O_{3(20\%)}$/AC_{nano}	44.49	634.76	0.61	130/634/800	214.39/1019.17/16 247.95	546	3510.07
$Co_3O_{4(15\%)}$–$La_2O_{3(20\%)}$/AC_{nano}	46.23	514.36	0.57	138/819/842	249.84/1191.16/18 843.94	906	3865.96
$Co_3O_{4(20\%)}$–$La_2O_{3(20\%)}$/AC_{nano}	48.41	501.79	0.52	135/609/831	254.21/4042.96/26 165.70	939	5292.06
$Co_3O_{4(25\%)}$–$La_2O_{3(20\%)}$/AC_{nano}	53.18	486.13	0.41	140/713/832	251.25/713.16/4400.43	901	3272.65

[a] The crystallite size was determined from the highest intensity line broadening of the XRD peak at $2\theta = 43.1°$. [b] BET surface area. [c] NH$_3$/CO$_2$ desorption peak for all the catalysts.

sites, it is speculated that elevated Co dosages of >20% will result in lower DO activity. Based on the result obtained, it is expected that the most effective ratio for converting WCO to hydrocarbon-like structures *via* DO is the $CoO_{(20\%)}$–$La_2O_{3(20\%)}$/AC_{nano} catalyst.

Since the $Co_3O_{4(20\%)}$–$La_2O_{3(20\%)}$/AC_{nano} catalyst showed superior acid-base active sites, a detailed study on its surface was performed *via* XPS analysis. Fig. S1A–E† reveal the deconvolution peaks at a binding energy (BE) of 284.7–289.8 eV (C), 531.8–533.1 eV (O) and ~133.7–135.7 eV (P) together with the characteristic peaks for La 3d$_5$ and Co 2p$_3$. The O 1s spectra for the $Co_3O_{4(20\%)}$–$La_2O_{3(20\%)}$/AC_{nano} catalyst present two peaks with the BE values of 529.8 eV, 531.8 eV and 533.1 eV (Fig. S1B†). The XPS peak at 529.8 eV is attributed to the lattice O^{2-} species, O_2^{2-}/O, whereas the peak at 531.6 eV originated from the

hydroxyl species, OH$^-$. The highest BE level peak at 533.10 eV is assigned to molecular water adsorbed on the surface of the catalyst.[44,45] This implies that the lanthanum and cobalt are in the form of oxides on the catalyst surface. It noteworthy to mention that the O 1s region showed the lowest BE peak compared to other elemental species, which are known to be less electron-rich oxygen species.[44] This is in agreement with surface atomic ratio data shown in Table 4, where only 6% O was detected on the $Co_3O_{4(20\%)}$–$La_2O_{3(20\%)}$/AC_{nano} catalyst. This result is also in accordance with the FESEM-EDX result, where only ~5% O was detected (Table 2). Thus, this finding confirms that the $Co_3O_{4(20)}$–$La_2O_{3(20)}$/AC_{nano} catalyst is comprised mainly of bimetallic Co–La alloy supported on AC_{nano}. The carbon in the $Co_3O_{4(20)}$–$La_2O_{3(20)}$/AC_{nano} catalyst was detected in the C 1s spectra (Fig. S1C†). Four distinct peaks were obtained at BE of
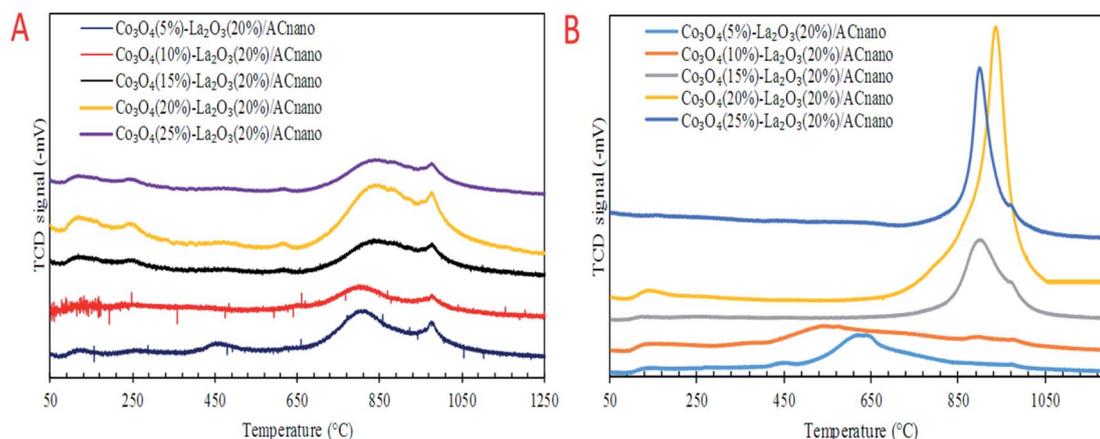

Fig. 3   (A) TPD-NH$_3$ and (B) TPD-CO$_2$ profiles for the $Co_3O_{4(x)}$–$La_2O_{3(20)}$/AC_{nano} catalysts.

Table 4 XPS peak deconvolution result in %, peak position, FWHM and surface concentration for the $Co_3O_{4(20\%)}$–$La_2O_{3(20\%)}AC_{nano}$ catalyst

State of element	O 1s			C 1s				Co 2p	La 3d$_5$	P 2p
Atomic percent (at%)	6.1			45.2				18.8	19.9	9.9
	O 1s. cf1	O 1s. cf2	O 1s. cf3	C–O	C–C	C=O	C(O)O	Co 2p$_{1/2}$		P 2p$_{3/2}$
Peak position (eV)	529.81	531.83	533.10	285.81	284.70	286.90	289.81	797.80	835.60	133.72
FWHM	1.42	1.80	196	1.42	1.26	1.57	1.55	2.96	—	2.12
Concentration (%)	16.35	56.55	27.09	27.98	55.69	10.87	5.47	—	—	—

284.7, 285.8, 286.9 and 289.8 eV. These peaks are attributed to C–C, C–O, C=O and C(O)O, respectively, demonstrating that three types of functional groups were incorporated during the synthesis of the catalyst. The value for C 1s belonging C–C was the highest (56%), implying that the AC_{nano} support is mainly composed of carbon-based material, which was connected by C–C bonds. The total C content was relatively high (45%), and thus enhanced the thermally stability of the catalyst at high reaction temperatures.[46] Referring to Fig. S1D,† the BE for the deconvolution curves of Co 2p were observed in the range of 781.9 eV (Co 2p$_{3/2}$) to 797.8 eV (Co 2p$_{l/2}$). This is evidence of the existence of cobalt metal on the catalyst surface. The significant deconvolution curves of Co 2p suggest that the cobalt metal was well distributed on the external AC surface, and it is speculated that the improvement in DO catalytic activity is due to the greater cobalt dispersion on the AC.[47] Fig. S1E† indicates deconvolution of the high-resolution P 2p spectra into a single peak, with binding energies of 133.7 eV for P 2p$_{3/3}$ and 135.3 eV for P 2p$_{1/2}$. These observations are linked to the presence of PO_4^{3-}, which was derived from the phosphate precursor of H_3PO_4 used in the chemical activation of the walnut shell.[25] Fig. S1F† indicates the presence of two regions displayed by La 3d$_5$ in lanthanum oxide (838.3 eV and 835.2 eV), which are associated with La^{3+} species on the catalyst surface.[48] Notably, the XPS results revealed a significant bonding interaction between Co^{2+} and La^{3+} in terms of a shift in the binding energies of Co 2p$_{3/2}$ (from 779.2 (Co_3O_4, standard) to 781.7), and a shift in the binding energy of La 3d$_5$ (from 834.5 eV (La_2O_3, standard) to 835.6 + 0.1 eV).[44,49] The shift in bond energy is also due to the formation of the bimetallic (La–Co) phase. The metallic bonding of La and Co was substantiated by the XRD results (refer to XRD).

3.2 DO of WCO over $Co_3O_{4(x)}$–$La_2O_{3(y)}$/AC_{nano} catalysts and effect of reaction atmosphere

The catalytic DO of WCO over the $Co_3O_{4(x)}$–$La_2O_{3(y)}$/AC_{nano} catalysts was conducted at a constant temperature (300 °C), for 1 h, with 0.5 wt% catalyst loading under two different conditions: (i) N_2 flow and (ii) closed system. The detailed GC-FID results are shown in Fig. 4. For comparison, a blank experiment was carried out over the AC_{nano} support. The results showed that the deoxygenized liquid products produced from both reaction systems were composed of saturated and unsaturated hydrocarbon fractions in the range of C_8–C_{20} (Fig. 4A). Notably, AC_{nano} had lower activity for the DO of WCO than the $Co_3O_{4(x)}$–$La_2O_{3(20\%)}$/AC_{nano} catalysts. The DO profile showed

that a low hydrocarbon yield (12–14%) was achieved from AC_{nano} catalysing DO in both reaction systems. However, when the $Co_3O_{4(20\%)}$–$La_2O_{3(20\%)}$/AC_{nano} catalyst was applied, high activity was observed with a hydrocarbon yield in range of 25–38%. The yields of liquid hydrocarbon were significantly increased in the order of $Co_3O_{4(20\%)}$–$La_2O_{3(20\%)}$/AC_{nano} > $Co_3O_{4(15\%)}$–$La_2O_{3(20\%)}$/AC_{nano} > $Co_3O_{4(25\%)}$–$La_2O_{3(20\%)}$/AC_{nano} > $Co_3O_{4(10\%)}$–$La_2O_{3(20\%)}$/AC_{nano} > $Co_3O_{4(5\%)}$–$La_2O_{3(20\%)}$/AC_{nano} > AC_{nano}. The hydrocarbons yield increased from 33–65% to 27–35% as the Co dopant increased from 5 to 20 wt% and reduced for 25 wt% Co concentration.

Theoretically, the WCO was composed majority of ~46% C_{16} and ~52% C_{18} fatty acids, which were further deoxygenized via decarboxylation/decarbonylation (deCOx) pathways to produce hydrocarbon fractions mainly of n-C_{15} and n-C_{17}. Fig. 4B and C shows the carbon distribution of the deoxygenated liquid product obtained from both DO systems. Considering that n-(C_{15} + C_{17}) was significantly found among the hydrocarbon products in all cases, it is conceivable that the n-(C_{15} + C_{17}) obtained resulted from the decarbonylation (deCOx) synthesis pathway. As the Co content increased, the deCOx rate increased and resulted in formation of n-(C_{15} + C_{17}) fractions.[50] In addition, the total selectivity of n-(C_{15} + C_{17}) was reduced (~29–41%) when 25 wt% of Co catalysed the reaction. Although some studies acknowledged that high deCOx activity is dominated by catalysts with rich weak + medium acidic sites (TPD-NH_3 desorption temperature <500 °C),[25,51,52] it was difficult to correlate this finding since the weak acid obtained from all the catalysts was close in value (Table 3). The high hydrocarbon yield (25–38%) and n-(C_{15} + C_{17}) fractions (36–65%) over the $Co_3O_{4(20\%)}$–$La_2O_{3(20\%)}$/AC_{nano} catalyst suggest that the DO activity via deCOx pathways was strongly affected by the surface density of strong acid and basic sites. This indicates that a higher degree of DO occurs over highly acidic and basic catalysts. The pronounced effect of acid-base characteristics in promoting the DO reaction is consistent with our previous investigations. The DO of WCO on Ag_2O–La_2O_3/AC_{nano} and CaO–La_2O_3/AC catalysts suggested that deCOx is favoured by the existence of a large amount of acid-based sites.[3,12]

As expected there was a great difference in the hydrocarbon fraction distribution between the DO reaction using the micro-batch closed system and reaction under N_2 flow. The DO of WCO under an N_2 flow gave a low hydrocarbon yield (25%) and also poor deCOx activity with only 36% n-(C_{15} + C_{17}) selectivity. Meanwhile, the n-(C_{15} + C_{17}) selectivity was found to increase significantly in the micro-batch closed system, with 38%
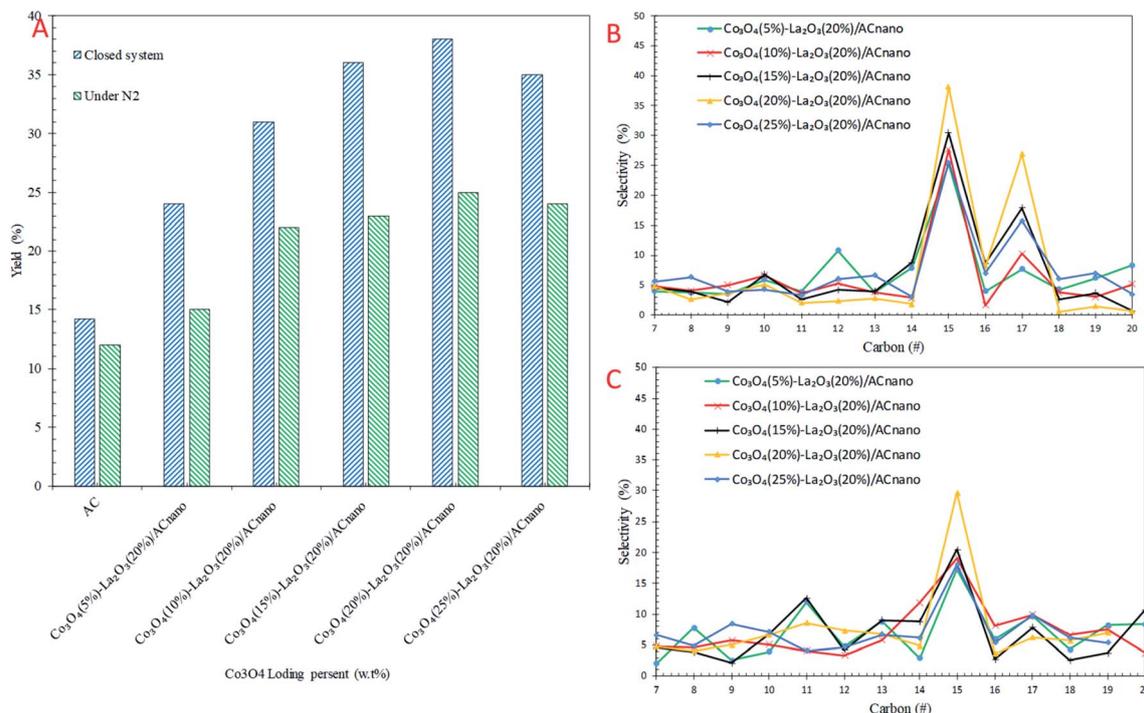
Fig. 4 (A) Effect of Co concentration from 5–25 wt% on (A) hydrocarbon yield, (B) selectivity toward C_8–C_{20} of the micro-batch closed system and (C) selectivity toward C_8–C_{20} under inert conditions with the reaction conditions of 0.5 wt% of catalyst loading, 1 h at 300 °C.

hydrocarbon yield and 68% n-(C_{15} + C_{17}) selectivity. This indicates that the deCOx reaction was promoted by the catalytic reaction under the high pressure built-up in the micro-batch closed system. In addition, this suggests competitive activation of the active sites by the high pressure DO system, which led to an enhancement in the deCOx reaction. The low selectivity toward n-(C_{15} + C_{17}) was prominent for DO catalysed by $Co_3O_{4(x)}$–$La_2O_{3(y)}$/AC_{nano} under an N_2 flow, which is due to the formation of rich oxygen-containing compounds (oxygenates and CO_2/CO gases) during the ineffective DO reaction. These

oxygenates can act as poisons by strongly adsorbing on the catalyst surface and deactivate the active sites of the catalyst.

The efficacy of WCO DO under the closed and N_2 flow systems over the $Co_3O_{4(20\%)}$–$La_2O_{3(20\%)}$/AC_{nano} catalysts was further confirmed by GCMS, as shown in Fig. 5A. It was observed that the DO of WCO in the micro-batch closed system produced a hydrocarbon fraction two times larger than that in the N_2 flow system. Interestingly, the peaks for carboxylic acids could not be observed in the deoxygenated liquid product from the micro-batch closed system, where in contrast the N_2 flow system produced >8% carboxylic acid. Moreover, the amount of
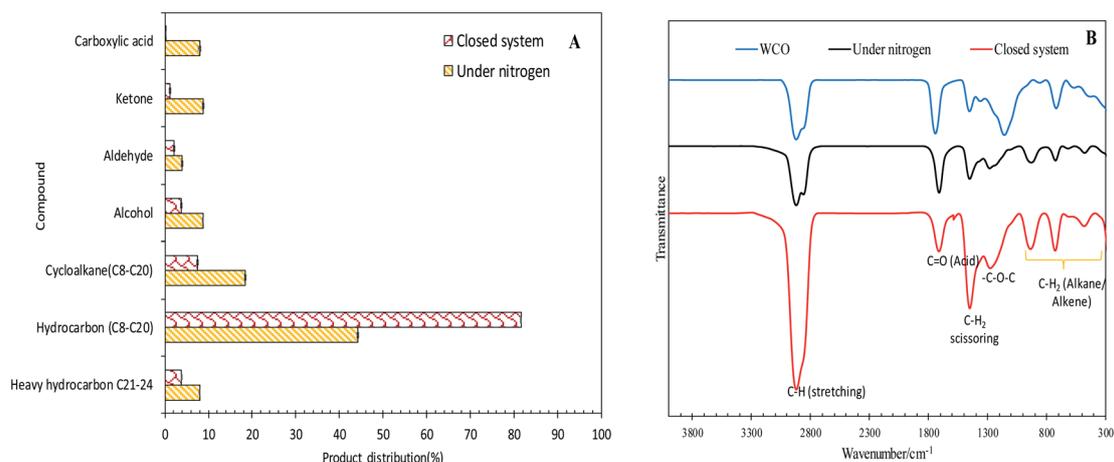

Fig. 5 (A) Product distribution of deoxygenated liquid product analysed by GC-MS and (B) FTIR spectra of the deoxygenized liquid product under the reaction conditions of $Co_3O_{4(20\%)}$–$La_2O_{3(20\%)}$/AC_{nano}, 0.5 wt% catalyst loading, 1 h reaction time, and 300 °C reaction temperature.

other oxygenate species such as ketones, aldehydes and alcohols was remarkably reduced (7.13%) in the micro-batch closed system. Thus, it can be concluded that the $Co_3O_{4(20\%)}$–$La_2O_{3(20\%)}$/AC_{nano} catalyzed DO in the micro-batch closed system offers successive cracking reactions via C–O cleavage, producing rich hydrocarbon fuel mixtures. The FTIR analysis was performed to study the chemical functional groups of the WCO (feedstock) and deoxygenized liquid products (Fig. 5B). The FTIR spectrum of WCO showed absorption bands at 2915 cm^{-1} (–CH), 1692 cm^{-1} (–C=O) stretching, 1447 cm^{-1} (–CH$_2$) scissoring, 1285 cm^{1} (–C–O–C) and 726 cm^{-1} (–(CH)$_n$-bending for alkane).[3] The FTIR results for WCO and the liquid deoxygenated product show that all the spectra were normalized by the intensity of the absorption band centered at 2753–3000 cm^{-1} (CH stretching, aliphatic). It is noteworthy that the liquid deoxygenated products showed a significant intensity reduction for the absorption band at 1692 cm^{-1}, which belongs to C=O (fatty acid), and the absence of C–O–C (from carbonyl group in WCO) absorption features at 1285 cm^{-1}. This result indicates the removal of oxygen species via deCOx pathways.[53,54] The DO close system exhibited a significantly lower intensity for the C=O and C–O–C peaks compared to DO in the N$_2$ flow system under the same experimental conditions.

3.3 Optimization studies

The effects of the $Co_3O_{4(20\%)}$–$La_2O_{3(20\%)}$/AC_{nano} catalyst loading (0.5 wt% to 5 wt%) towards hydrocarbon yield and product selectivity at 300 °C temperature and 60 min reaction time under inert conditions and in the micro-batch closed system with a stirring speed of 400 rpm are shown in Fig. 6A–C. The results show that the DO activity increased with an increment in catalyst loading within the range of 0.5 wt% to 1 wt%, which yielded 43% and 35% of hydrocarbons with 69% and 47% n-C$_{15}$ + n-C$_{17}$ selectivity for the reaction using the micro-batch closed system and under N$_2$ flow, respectively. This finding is possibly due to the fact that the increase in the catalyst loading enhanced the exposure of active sites for the accessibility of the feedstock in the DO reaction.[55] However, a further increase in the catalyst loading to >1 wt% resulted a reduction in hydrocarbon yield to <40% and n-C$_{15}$ + n-C$_{17}$ selectivity to <43% in both DO systems. This is due to the occurrence of parallel or secondary reactions, such as polymerization pathways. The excess active sites due to a high catalyst loading increased the rapid-rate reaction on the catalyst surface, which simultaneously resulted in shortening of the catalyst life span by coke formation caused by polymerization reaction.[56] In the present study, 1 wt% catalyst loading was observed to be optimal for the catalytic DO reaction.
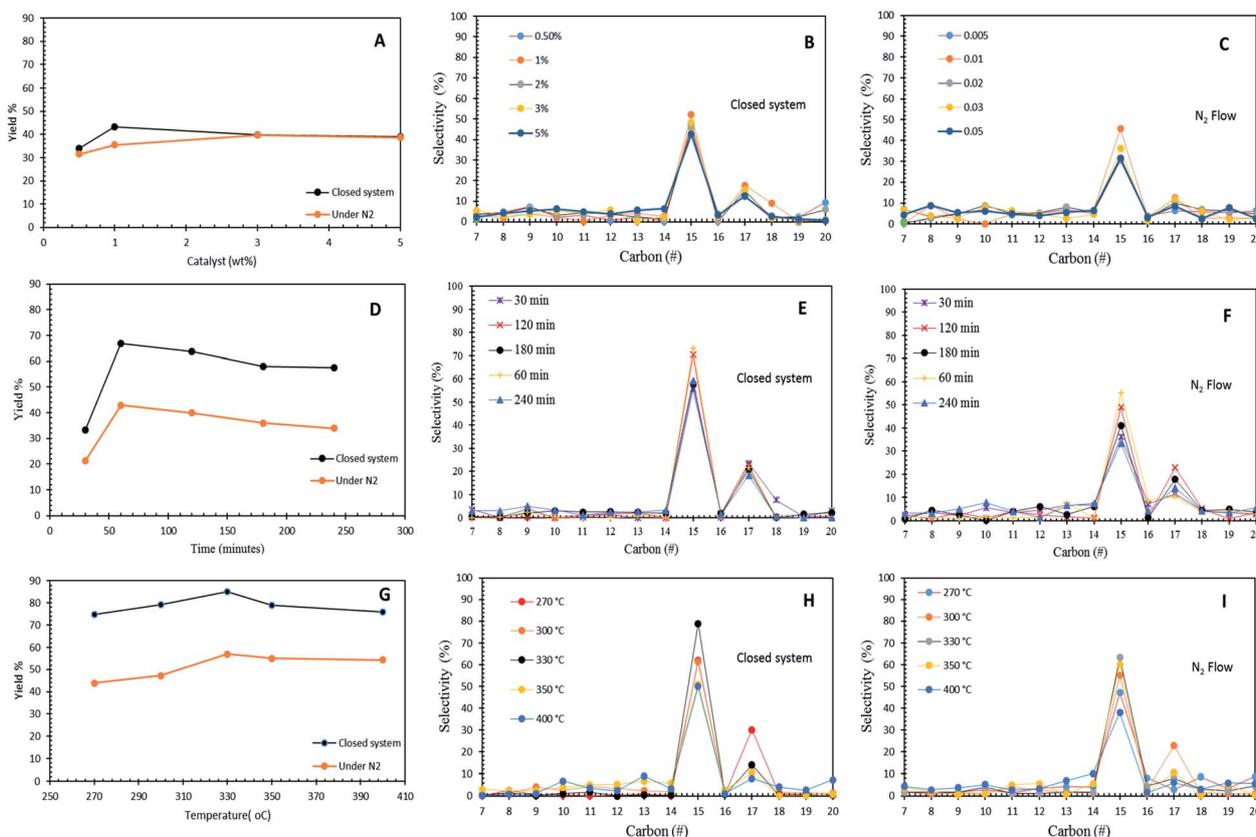

Fig. 6 Optimization studies of WCO, (A–C) DO reactions of $Co_3O_{4(20\%)}$–$La_2O_{3(20\%)}$/AC_{nano} catalyst affected by catalyst amount; reaction conditions: 300 °C and 1 h. (D–F) DO reactions of $Co_3O_{4(20\%)}$-$La_2O_{3(20\%)}$/AC_{nano} catalyst affected by reaction time; reaction conditions: 1 wt% catalyst loading and 330 °C. (G–I) DO reactions of $Co_3O_{4(20\%)}$–$La_2O_{3(20\%)}$/AC_{nano} catalyst affected by reaction temperature; reaction conditions: 1 wt% catalyst loading, 1 h for 400 rpm under an N$_2$ flow and micro-batch closed system.

Fig. 6D–F show the effect of reaction time in the range of 30 min to 240 min with 1 wt% $Co_3O_{4(20\%)}$–$La_2O_{3(20\%)}$/AC_{nano} catalyst loading at a temperature of 300 °C in the micro-batch closed system and inert N_2 flow condition. The results showed that the DO activity depends on the reaction time. As the reaction time increased from 30 min to 60 min, the hydrocarbon yield increased from 33% to 66% and 21% to 39% for DO in the micro-batch closed system and inert condition, respectively. Meanwhile, the closed and inert N_2 flow system also showed an increment of n-C_{15} + n-C_{17} selectivity from 79% to 94%, and 47% to 58%, respectively. Further prolonging the time to 240 min led to a slight reduction in the hydrocarbon yield from 66% to 57% and 39% to 34%, and the n-C_{15} + n-C_{17} selectivity was reduced to >77% and 47%, respectively. The insignificant changes in the hydrocarbon yield and n-C_{15} + n-C_{17} selectivity indicate that DO *via* deCOx reaction was highly unaffected in this time range. The lowest catalytic activity was observed at the longest reaction time (240 min), which is because unfavourable side reactions (*i.e.*, polymerization) occur during a longer reaction time. These side reactions accelerated the deactivation of the catalyst since the polymerization process generates coke on the catalyst. Coke formation reduces the effectiveness of the catalyst and leads to the accumulation of different compounds on the catalyst surface, covering the active sites, and thus suppressing the reaction at the catalytic centres of the catalyst.[57]

The effect of reaction temperature in the DO of WCO was investigated in the temperature range of 270 °C to 400 °C, with a $Co_3O_{4(20\%)}$–$La_2O_{3(20\%)}$/AC_{nano} catalyst loading of 1 wt%, and reaction time of 60 min in the micro-batch closed and inert N_2 flow system with a stirring speed of 400 rpm (Fig. 6G–I). The DO activity increased with an increase in temperature from 270 °C to 330 °C. Both DO systems showed a similar trend of activity, whereby the highest catalytic activity was found at a temperature of 330 °C. This proves that $Co_3O_{4(20\%)}$–$La_2O_{3(20\%)}$/AC_{nano} is thermally stable since it is capable to withstand at a high temperature. A further increase in temperature to >330 °C led to the retardation of catalytic activity with a lower hydrocarbon yield and n-C_{15} + n-C_{17} selectivity. The high reaction temperature enhanced the occurrence of cracking *via* C–C scission in the triglycerides and n-C_{15} + n-C_{17} fractions into lighter fractions.[58] Therefore, the formation of lighter fractions (*i.e.*, gaseous products) and gasoline fraction (*i.e.*, C_8–C_{12}) simultaneously reduced the hydrocarbon yield and n-C_{15} + n-C_{17} selectivity. In this study, the optimum reaction temperature in the N_2 flow system was achieved at 330 °C, 1 wt% catalyst within 60 min, with 52% hydrocarbon yield and 71% n-C_{15} + n-C_{17} selectivity. On the other hand, the optimum catalytic DO (hydrocarbon yield = 85%, n-C_{15} + n-C_{17} = 93%) was achieved within 60 min and 1 wt% catalyst loading at 330 °C in the micro-batch closed system.

3.4 Effect of water and FFA content in DO of WCO

Other important factors affecting the DO activity are water and FFA content in the feedstock. It was reported in a previous study that the addition of water to the DO feedstock produced three beneficial effects: (1) low acidic and other low-value oxygenated components, (2) prevent the beneficial components that are partially miscible in water to not easily be excluded from DO; and (3) in particularly strong catalysts, water regulates the catalyst site interactions with the feedstock components.[59] The investigation of the content of water and FFA on the DO of WCO over the $Co_3O_{4(20\%)}$–$La_2O_{3(20\%)}$/AC_{nano} catalyst was performed using the optimum parameters of 1 wt%, 60 min at 330 °C in the micro-batch closed system. All the obtained results are displayed in Fig. S2A–D.† Some publications suggest the negative impact of water towards DO activity, where water results in the modification of the external catalyst surface, simultaneously leading to the loss of some active metals species, and reduces the catalytic DO activity. Interestingly, the impact of water on the DO of WCO over the $Co_3O_{4(20\%)}$–$La_2O_{3(20\%)}$/AC_{nano} catalyst showed a positive effect (Fig. S2A and B†). In the present study, increasing the water content from 1 wt% to 5 wt% resulted in an increase in the hydrocarbon yield from 82% to 88%, while the n-C_{15} + n-C_{17} selectivity increased from 90% to 93%. This indicates that the addition of water to WCO facilitated the C–O cleavage of fatty acids *via* the deCOx reaction. The hydrocarbon yield and selectivity reached ~88% and 93% n-C_{15} + n-C_{17} when the water content was >5 wt%, respectively. This indicates that the cobalt and lanthanum supported on AC_{nano} were chemically and thermally stable at high temperature even with a large amount of water in the feedstock.

Further study on the effect of FFAs towards the DO reaction was performed. Since the WCO consisted mainly of C_{18} of fatty acids, oleic acid (C_{18}) was chosen as a model reactant. The FFA% of the WCO was controlled by further adding commercial oleic acid as a representative natural FFA. The FFA% for the feedstock mixture (WCO + oleic acid) used was in the range of 18% to 38% (Fig. S2C and D†). It was found that all the feedstocks were effectively deoxygenized *via* the selective deCOx reaction with a higher percentage of hydrocarbon fraction of >93%, and the product was predominantly selective toward n-C_{15} + n-C_{17} fractions. The total hydrocarbons was found to increase from 88% to 96% with an increase in FFA content from 18% to 38%. In contrast, the value of n-C_{15} + n-C_{17} selectivity was reduced to 84% from 94%. The results suggest that an FFA-rich feed encourages C–C cleavage rather than C–O cleavage. Evidently, n-C_9, n-C_{12} and n-C_{13} were found to be prominent in the DO of the FFA-rich feedstocks (FFA > 23%). It has been reported that a higher content of FFA in the feedstock will lead to a decrease in DO activity and favour the cracking reaction. Overall, the DO of the FFAs–WCO mixtures was still favorable toward C–O cleavage and produced rich diesel-like fuels. This suggests the $Co_3O_{4(20\%)}$–$La_2O_{3(20\%)}$/AC_{nano} catalyst is highly adaptable to water–FFA conditions in the DO process, and thus it can be applied for other realistic feedstocks.

3.5 Reusability of $Co_3O_{4(20\%)}$–$La_2O_{3(20\%)}$/AC_{nano} catalyst

The reusability profile of the $Co_3O_{4(20\%)}$–$La_2O_{3(20\%)}$/AC_{nano} catalyst was investigated *via* DO reaction in the micro-batch closed system condition under the conditions of 1 wt% catalyst at 330 °C within 60 min (Fig. S3A†). Upon the completion of each cycle, the catalyst was reactivated by simple washing with

Table 5 Comparison study on catalytic DO with various feeds

No.	Catalyst	Support	Reaction	Feed	FFA (%)	Reaction condition	H/C (yield%)	Selectivity (%)	Reusability	Coke (wt%)	Reference
1	Ni–Ag/AC$_{CFR}$	Coconut fibre residue	DO	JCO	15.4	Catalyst loading: 5 wt% Temperature: 350 °C Time: 1 h under N$_2$ flow	80	83 (n-C$_{15}$ + C$_{17}$)	5	2.5	11
2	CaO–La$_2$O$_3$/AC	Walnut shell	DO	WCO	18.4	Catalyst loading: 3 wt% Temperature: 330 °C, Time: 3 h under N$_2$ flow	72	82 (n-C$_{15}$ + C$_{17}$)	6	2	5
3	Ag$_2$O$_3$–La$_2$O$_3$/AC$_{nano}$	Walnut shell	DO	WCO	18.4	Catalyst loading: 1 wt% Temperature: 350 °C Time: 2 h under N$_2$ flow	89	93 (n-C$_{15}$ + C$_{17}$)	6	1.3	6
4	Co$_3$O$_{4(20\%)}$–La$_2$O$_{3(20\%)}$/AC$_{nano}$	Walnut shell	DO	WCO	38.4	Catalyst loading: 1 wt% Temperature: 330 °C Time: 1 h and 5% of water content	96	93 (n-C$_{15}$ + C$_{17}$)	8	3.7	Present study

hexane and reused for the next cycle. The results showed that the Co$_3$O$_{4(20\%)}$–La$_2$O$_{3(20\%)}$/AC$_{nano}$ catalyst performed steadily for eight consecutive runs, maintaining the hydrocarbon yield at >72% with >80% selectivity of C$_{15}$ and C$_{17}$ products (Fig. S3A and S4†). This indicates that the Co$_3$O$_{4(20\%)}$–La$_2$O$_{3(20\%)}$/AC$_{nano}$ catalyst possesses mechanical properties and chemical stability. Furthermore, the elemental study indicated a negligible amount of La^{3+} and Co^{4+} species leached from the Co$_3$O$_{4(20\%)}$–La$_2$O$_{3(20\%)}$/AC$_{nano}$ catalyst during each reaction. The comparison study show that the leached La^{3+} and Co^{4+} in the liquid product of the fresh and 8th-run catalyst gradually increased from 1 ppm to 3 ppm and 1 ppm to 4 ppm, respectively. Hence, the loss in DO activity is due to the dissolution of the active metals during continuous runs. Furthermore, the leaching level is within the maximum range of the EN 12662 Standard Specification for Diesel Fuel Oils contamination content (24 mg L^{-1}),[60] which confirms that the Co$_3$O$_{4(20\%)}$–La$_2$O$_{3(20\%)}$/AC$_{nano}$ catalyst shows potential leaching resistance and exhibits good stability.

The metal dispersion states and chemical composition study for the Co$_3$O$_{4(20\%)}$–La$_2$O$_{3(20\%)}$/AC$_{nano}$ catalyst (fresh and spent catalysts) were determined by XRD and TGA analysis (Fig. S3B and C†), respectively. The XRD analysis showed that the spent catalysts exhibited similar bimetallic active CoLaO$_3$ phases with higher crystallinity at 2θ = 23.3°, 40.2° and 69.9° (JCPDS File no. 00-006-0491). The crystallite size of the Co$_3$O$_{4(20\%)}$–La$_2$O$_{3(20\%)}$/AC$_{nano}$ particles evaluated at 2θ: 43.1 showed a minor change in the crystallite size of the spent catalyst (Fig. S3B†). The TGA analysis was performed to examine the extent of coke formation during the DO of WCO using the Co$_3$O$_{4(20\%)}$–La$_2$O$_{3(20\%)}$/AC$_{nano}$ catalyst. The results showed a decomposition peak in the temperature range of 290 °C to 550 °C. This is attributed to the combustion of the activated carbon nanorods. The initial decomposition temperature for the fresh and spent catalysts was similar; however, the final decomposition temperature for the spent catalyst was significantly higher >550 °C. Furthermore, the weight loss for the spent catalyst was 3.7 wt% higher than that of the fresh catalyst, which was due to the oxidation of coke in air (Fig. S3C†). The coke is categorized as hard coke,

which decomposed completely at a temperature >550 °C.[61] The deposited coke will accumulate on the catalyst surface, which covers the active sites on the catalyst and reduces the catalytic DO activity. The negligible loss in DO activity throughout eight reaction runs is an indication that coke formation had an insignificant effect on the active sites of the Co$_3$O$_{4(20\%)}$–La$_2$O$_{3(20\%)}$/AC$_{nano}$ catalyst, which confirms that the La$_2$O$_3$ and Co$_3$O$_4$ supported AC catalyst exhibits high stability. Notably, the use of carbon as a support in the DO reaction has been widely explored due to its excellent thermal stability. For instance, the use of a bimetallic doped carbon catalyst in the DO of non-edible oil including jatropha oil and WCO was recently explored by our group.[5,6,11] Ni–Ag/AC, CaO–La$_2$O$_3$/AC, and Ag$_2$O$_3$–La$_2$O$_3$/AC$_{nano}$ were found to be effective in removing the oxygenated compound *via* deCO$_x$ pathways and yielded hydrocarbon in the range of 72–89% with product selectively toward n-C$_{15}$ + C$_{17}$ fractions (82–93%) and could be reused four to six times (Table 5). Notably, Co$_3$O$_{4(20\%)}$–La$_2$O$_{3(20\%)}$/AC$_{nano}$ exhibited excellent catalyst activity with hydrocarbon yield and selectivity of 96% and 93%, respectively. Moreover, the Co$_3$O$_{4(20\%)}$–La$_2$O$_{3(20\%)}$/AC$_{nano}$ catalyst showed high catalytic stability with eight times successive reusability with a hydrocarbon yield of >80% and n-C$_{15}$ + C$_{17}$ selectivity of >83%. Although the coke formed on the surface of Co$_3$O$_{4(20\%)}$–La$_2$O$_{3(20\%)}$/AC$_{nano}$ was more pronounced than that in previous studies, it still exhibited high stability, reusability and catalytic activity. This suggests by the presence of high acidic active sites with a high surface area and pore volume,[12] which are favorable for the DO reaction.

4. Conclusion

In the present work, an effective DO reaction was developed by converting triglyceride-based feeds to diesel-like fuel over the Co$_3$O$_{4(x)}$–La$_2$O$_{3(y)}$/AC$_{nano}$ catalyst. The improvement in the DO of WCO over the acid–base Co$_3$O$_{4(x)}$–La$_2$O$_{3(y)}$/AC$_{nano}$ catalyst was due to the neutralization of the strong acidic sites. DO using a micro-reactor closed system showed better reactivity compared to semi-batch inert flow conditions due to the

advantages of high pressure, which is beneficial in maintaining high catalytic activity. The cracking pathway was found to be enhanced with an increase in Co content due to the richness of the high-strength basic and acid sites of the $Co_3O_{4(x)}$–$La_2O_{3(y)}$/AC_{nano} catalyst. Among the Co contents (5–25 wt%), the optimum content of Co for deCOx activity is 20 wt%. The effects of reaction time, catalyst loading, temperature, water and FFA content were further investigated with the optimum DO condition (hydrocarbon fraction = 96%, n-C_{15} + n-C_{17} = 93%) achieved using 1 wt% catalyst loading within 60 min at 330 °C, 38.4 wt% FFA and 5% water content in the micro-batch closed system. The efficiency of the $Co_3O_{4(20\%)}$–$La_2O_{3(20\%)}$/AC_{nano} catalyst was proven to be capable of deoxygenizing low quality feedstocks with a high FFA (38%) and high water content (5 wt%) under the optimum conditions. The $Co_3O_{4(20\%)}$–$La_2O_{3(20\%)}$/AC_{nano} catalyst showed high stability and reusability up to eight times with the yield and selectivity maintained at >72% and >80% for n-C_{15} + C_{17}.

Conflicts of interest

There are no conflicts to declare.

Acknowledgements

References

1 S. H. H. Al-jaberi, U. Rashid, F. A. J. Al-doghachi and G. Abdulkareem-alsultan, *Energy Convers. Manage.*, 2017, **139**, 166–174.

2 A. Alsultan, N. Asikin-mijan and T. Y. Yun Hin, *Mater. Sci. Forum*, 2016, **840**, 348–352.

3 G. Abdulkareem-Alsultan, N. Asikin-Mijan, H. V. Lee, A. S. Albazzaz and Y. H. H. Taufiq-Yap, *Energy Convers. Manage.*, 2017, **151**, 311–323.

4 P. Mäki-Arvela, M. Snåre, K. Eränen, J. Myllyoja and D. Y. Murzin, *Fuel*, 2008, **87**, 3543–3549.

5 H. Dietz, L. Dittmar, D. Ohms, M. Radwan and K. Wiesener, *US Pat.*, 6,285,167, 2001.

6 A. E. Barrón C., J. A. Melo-Banda, J. M. Dominguez E., E. Hernández M., R. Silva R., A. I. Reyes T. and M. A. Meraz M., *Catal. Today*, 2011, **166**, 102–110.

7 P. Hongmanorom, A. Luengnaruemitchai, N. Chollacoop and Y. Yoshimura, *Energy Fuels*, 2017, **31**, 8202–8209.

8 Y. Rezgui and M. Guemini, *Appl. Catal., A*, 2005, **282**, 45–53.

9 H. Zhang, H. Lin and Y. Zheng, *Appl. Catal., B*, 2014, **160–161**, 415–422.

10 N. Asikin-Mijan, H. V. Lee, J. C. Juan, A. R. Noorsaadah, H. C. Ong, S. M. Razali and Y. H. Taufiq-Yap, *Appl. Catal., A*, 2018, **552**, 38–48.

11 N. Asikin-Mijan, H. V. Lee, J. C. Juan, A. R. Noorsaadah and Y. H. Taufiq-Yap, *RSC Adv.*, 2017, **7**, 46445–46460.

12 G. Abdulkareem-Alsultan, N. Asikin-Mijan, N. Mansir, H. V. Lee, Z. Zainal, A. Islam and Y. H. Taufiq-Yap, *J. Anal. Appl. Pyrolysis*, 2018, **137**, 171–184.

13 M. Benito, S. Garc, L. Garc and L. Daza, *Acc. Chem.*, 2007, **169**, 177–183.

14 M. Kashid, O. Detraz, M. S. Moya, I. Yuranov, P. Prechtl, J. Membrez, A. Renken and L. Kiwi-Minsker, *Chem. Eng. J.*, 2013, **214**, 149–156.

15 R. Abdallah, B. Fumey, V. Meille and C. de Bellefon, *Catal. Today*, 2007, **125**, 34–39.

16 M. T. Janicke, H. Kestenbaum, U. Hagendorf, F. Schüth, M. Fichtner and K. Schubert, *J. Catal.*, 2000, **191**, 282–293.

17 M. Ueno, H. Hisamoto, T. Kitamori and S. Kobayashi, *Chem. Commun.*, 2003, **3**, 936–937.

18 N. Asikin-Mijan, H. V. Lee, G. Abdulkareem-Alsultan, A. Afandi and Y. H. Taufiq-Yap, *J. Cleaner Prod.*, 2016, **167**, 1–12.

19 B. Gurunathan and A. Ravi, *Bioresour. Technol.*, 2015, **188**, 124–127.

20 J. Sahira and P. P. Bhadra, *J. Inst. Eng.*, 2013, **9**, 79–88.

21 S. Yorgun and D. Yıldız, *J. Taiwan Inst. Chem. Eng.*, 2015, **53**, 122–131.

22 L. N. Silva, I. C. P. Fortes, F. P. De Sousa and V. M. D. Pasa, *Fuel*, 2016, **164**, 329–338.

23 V. P. Dinesh, P. Biji, A. Ashok, S. K. Dhara, M. Kamruddin, A. K. Tyagi and B. Raj, *RSC Adv.*, 2014, **4**, 58930–58940.

24 B. Balusamy, B. E. Taştan, S. F. Ergen, T. Uyar and T. Tekinay, *Environ. Sci.: Processes Impacts.*, 2015, **17**, 1–10.

25 G. Abdulkareem-Alsultan, N. Asikin-Mijan, H. V. V. Lee and Y. H. Taufiq-Yap, *Chem. Eng. J.*, 2016, **304**, 61–71.

26 J. Wu, Q. Xia, H. Wang and Z. Li, *Appl. Catal., B*, 2014, **156–157**, 265–272.

27 E. W. Qian, N. Chen and S. Gong, *J. Mol. Catal. A: Chem.*, 2014, **387**, 76–85.

28 H. Imai, K. Takami and M. Naito, *Mater. Res. Bull.*, 1984, **19**, 1293–1300.

29 Z. Pan, R. Wang, M. Li, Y. Chu and J. Chen, *J. Energy Chem.*, 2015, **24**, 77–86.

30 Ş. Özkara, A. N. Akin, Z. Misirli and A. E. Aksoylu, *Turk. J. Chem.*, 2005, **29**, 219–224.

31 I. Khan, K. Saeed and I. Khan, *Arabian J. Chem.*, 2019, **12**, 908–931.

32 G. Abdulkreem-Alsultan, A. Islam, J. Janaun, M. S. Mastuli and Y. H. Taufiq-Yap, *Mater. Lett.*, 2016, **179**, 57–60.

33 A. M. Robinson, J. E. Hensley and J. Will Medlin, *ACS Catal.*, 2016, **6**, 5026–5043.

34 Z. Si, X. Zhang, C. Wang, L. Ma and R. Dong, *Catalysts*, 2017, **7**, 169.

35 S. Cheng, L. Wei, X. Zhao and J. Julson, *Catalysts*, 2016, **6**, 195.

36 A. Hakim, T. S. Marliza, N. M. Abu Tahari, R. W. N. Wan Isahak, R. M. Yusop, W. M. Mohamed Hisham and A. M. Yarmo, *Ind. Eng. Chem. Res.*, 2016, **55**, 7888–7897.

37 D. W. Lee, Y. M. Park and K. Y. Lee, *Catal. Surv. Asia*, 2009, **13**, 63–77.

38 A. Molaei Dehkordi and M. Ghasemi, *Fuel Process. Technol.*, 2012, **97**, 45–51.

39 P. A. L. Sheena, A. Sreedevi, C. Viji and V. Thomas, *Eur. Phys. J. B*, 2019, **92**, 1–8.

40 E. Laurent and B. Delmon, *Appl. Catal., A*, 1994, **109**, 77–96.

41 M. Sajdak, R. Muzyka, J. Hrabak and K. Słowik, *J. Anal. Appl. Pyrolysis*, 2015, **112**, 298–305.

42 T. V. Choudhary and C. B. Phillips, *Appl. Catal., A*, 2011, **397**, 1–12.

43 S. Lu, L. Wang, T. Qi, D. Qi, X. Xing, Y. Zhang, H. Xiao and S. Zhang, *J. Hazard. Mater.*, 2019, **365**, 531–537.

44 N. A. Merino, B. P. Barbero, P. Eloy and L. E. Cadus, *Appl. Surf. Sci.*, 2006, **253**, 1489–1493.

45 J. L. G. Fierro, *Catal. Today*, 1990, **8**, 153–174.

46 M. Haruta, N. Yamada, T. Kobayashi and S. Iijima, *J. Catal.*, 1989, **309**, 301–309.

47 M. Richard, F. Can, A. G. Fortu, A. Fendler, M. Alves-Fortunato, M. Richard, C. Wang, J. A. Díaz, S. Gil and Y. Guo, *Appl. Catal., B*, 2016, **180**, 29–37.

48 S. Yan, S. O. Salley and K. Y. Simon Ng, *Appl. Catal., A*, 2009, **353**, 203–212.

49 D. Mukai, S. Tochiya, Y. Murai, M. Imori, T. Hashimoto, Y. Sugiura and Y. Sekine, *Appl. Catal., A*, 2013, **453**, 60–70.

50 J. Zhang, Y. Bai, Q. Zhang, X. Wang, T. Zhang, Y. Tan and Y. Han, *Fuel*, 2014, **132**, 211–218.

51 Z. Zhong, H. Ang, C. Choong, L. Chen, L. Huang and J. Lin, *Phys. Chem. Chem. Phys.*, 2009, **11**, 872–880.

52 H. Dong, L. Zhang, Z. Fang, W. Fu, T. Tang, Y. Feng and T. Tang, *RSC Adv.*, 2017, **7**, 22008–22016.

53 J. K. Satyarthi and D. Srinivas, *Energy Fuels*, 2011, **25**, 3318–3322.

54 S. Zulkepli, J. Ching, H. Voon, N. Saadah, A. Rahman, J. C. Juan, H. V. Lee, N. S. A. Rahman, P. L. Show and E. P. Ng, *Energy Convers. Manag.*, 2018, **165**, 495–508.

55 K. C. Kwon, H. May, T. Marolla, B. Nichols, M. Mashburn, H. Mayfield, T. Marolla, B. Nichols and M. Mashburn, *Renewable Energy*, 2011, **36**, 907–915.

56 Y. Boyjoo, M. Ang and V. Pareek, *Int. J. Photoenergy*, 2012, **2012**, 1–7.

57 M. Arend, T. Nonnen, W. F. Hoelderich, J. Fischer and J. Groos, *Appl. Catal., A*, 2011, **399**, 198–204.

58 S. Bezergianni, S. Voutetakis and A. Kalogianni, *Ind. Eng. Chem. Res.*, 2009, **48**, 8402–8406.

59 Y. Elkasabi, C. A. Mullen, A. L. M. T. M. T. Pighinelli and A. A. Boateng, *Fuel Process. Technol.*, 2014, **123**, 11–18.

60 J. Bacha, J. Freel, A. Gibbs, L. Gibbs, G. Hemighaus, K. Hoekman, J. Horn, M. Ingham, L. Jossens, D. Kohler, D. Lesnini, J. McGeehan, M. Nikanjam, E. Olsen, R. Organ, B. Scott, M. Sztenderowicz, A. Tiedemann, C. Walker, J. Lind, J. Jones, D. Scott and J. Mills, *Chevron Glob. Mark.*, 2007, pp. 1–117.

61 S. K. Sahoo, S. S. Ray and I. D. Singh, *Appl. Catal., A*, 2004, **278**, 83–91.